

Wall speed and shape in singlet-assisted strong electroweak phase transitions

Avi Friedlander,^{1,*} Ian Banta,^{2,†} James M. Cline,^{3,‡} and David Tucker-Smith^{2,§}

¹*Queen's University, Department of Physics & Engineering Physics
Astronomy Kingston, Ontario, K7L 3N6 Kingston, Canada*

²*Department of Physics, Williams College, Williamstown, MA 01267*

³*McGill University, Department of Physics, 3600 University St., Montréal, QC H3A2T8 Canada*

(Dated: August 2020)

Models with singlet fields coupling to the Higgs can enable a strongly first order electroweak phase transition, of interest for baryogenesis and gravity waves. We improve on previous attempts to self-consistently solve for the bubble wall properties—wall speed v_w and shape—in a highly predictive class of models with Z_2 -symmetric singlet potentials. A new algorithm is implemented to determine v_w and the wall profiles throughout the singlet parameter space in the case of subsonic walls, focusing on models with strong enough phase transitions to satisfy the sphaleron washout constraint for electroweak baryogenesis. We find speeds as low as $v_w \cong 0.22$ in our scan over parameter space, and the singlet must be relatively light to have a subsonic wall, $m_s \lesssim 110$ GeV.

I. INTRODUCTION

The electroweak phase transition (EWPT) in the early universe has been intensively studied as a possible source for the cosmic baryon symmetry and gravitational waves. Within the standard model (SM) neither of these interesting outcomes are possible, given the known mass of the Higgs boson, because the phase transition is a smooth crossover [1, 2], whereas a first-order EWPT is required for electroweak baryogenesis (EWBG) and production of observable gravity waves (for reviews, see for example refs. [3, 4]). New physics, typically in the form of scalar fields coupling to the Higgs boson, can however lead to a first-order transition, with consequent nucleation of bubbles of the true (electroweak symmetry broken) vacuum, at the onset of the transition.

In order to make quantitative predictions for either baryogenesis or gravitational wave production in a given model, it is necessary to understand the detailed properties of the phase transition bubbles, especially the shape of the bubble walls (typically modeled as a tanh with some thickness L_w) and the terminal velocity v_w attained by them, once the forces of internal pressure and external friction from the plasma have balanced each other. This calculation, first carried out for the SM in refs. [5–7] (assuming a light Higgs boson), and in the Minimal Supersymmetric Standard Model, where the phase transition is enhanced by light stops, in refs. [8, 9],

turns out to be quite challenging because the frictional force, which requires solving the Boltzmann equations for the perturbations of the plasma caused by the wall, depends on the same wall properties that one is trying to determine.

A self-consistent procedure to solve this system is numerically expensive, and for this reason many studies of EWBG or gravitational wave production leave L_w and v_w as phenomenological parameters that can be freely varied, or in a somewhat better approximation, calculated by modeling the friction in a phenomenological way [10–12]. However to assess the prospects for a specific model to yield interesting results, one must eventually carry out the actual computation of L_w and v_w with the actual friction term derived from the fluid perturbations. Accurate estimates of these parameters are needed to make quantitative predictions for baryogenesis or gravity wave production.

The procedure becomes even more laborious in the case where an extra singlet field couples to the Higgs, in order to facilitate the first order transition, and also gets a vacuum expectation value (VEV) in the bubble wall [13, 14]. In that case one must solve for both field profiles, which has been attempted in refs. [15, 16], subject to some limiting approximations. In particular, these previous works assumed that the bubble wall shapes are described by tanh profiles. In reality, the Higgs field and the singlet can have shapes that differ from such an assumption, and it is not obvious how strongly this affects the determination of v_w . One of our main purposes is to overcome this limitation by developing an algorithm to determine the actual wall profiles along with v_w .

Moreover previous studies of singlet-assisted strong EWPTs have focused on a few benchmark models. In the present work we make a comprehen-

* avi.friedlander@queensu.ca

† banta@physics.ucsb.edu

‡ jcline@physics.mcgill.ca

§ dtuckers@williams.edu

sive scan of the parameter space for a class of models, where the singlet potential has the Z_2 symmetry $s \rightarrow -s$, and the singlet VEV disappears at low temperatures. This choice has the virtue of simplicity, being characterized by three parameters, the singlet mass m_s , its cross coupling λ_{hs} to the Higgs, and the VEV w_0 of s in the false vacuum where $h = 0$. The barrier between the true and false vacua provided by the $\lambda_{hs}h^2s^2$ interaction is already present at tree level, and is what enables the phase transition to be strongly first order [13, 14]. Moreover with $\langle s \rangle = 0$ at $T = 0$, the new sources of CP violation needed for EWBG are not overly constrained by experimental limits on electric dipole moments.

The paper is organized as follows. Section II describes the singlet scalar model used throughout the paper. Section III outlines the main features of the electroweak phase transition dynamics that will be studied in detail in the following. In section IV the methodology for determining the wall dynamics, including its velocity, are described; the results of those calculations are presented in section V. Conclusions are given in section VI. Appendices contain details concerning the finite-temperature effective potential (appendix A), diffusion equations used to determine the fluid perturbations (appendix B), and exceptional models that have peculiar features in their potentials (appendix C).

II. THE MODEL

A simple extension of the SM is the addition of a scalar singlet s that couples only to the Higgs field, and has the Z_2 symmetry $s \rightarrow -s$. Its zero-temperature tree level potential is given by

$$V_0 = \lambda_h \left(|H|^2 - \frac{1}{2}v_0^2 \right)^2 + \frac{1}{4}\lambda_s (s^2 - w_0^2)^2 + \frac{1}{2}\lambda_{hs}|H|^2s^2 \quad (1)$$

where H is the Standard Model Higgs doublet, and λ_h , v_0 are the Higgs self-coupling and VEV respectively. There are three new parameters λ_s , w_0 , and λ_{hs} , that describe the singlet's self coupling, its VEV when in the false minimum where $H = 0$, and the coupling between H and s . There is no loss of generality by omitting a separate $m_0^2s^2$ mass term. The physical singlet mass in the electroweak broken vacuum is given by

$$m_s^2 = -\lambda_s w_0^2 + \frac{1}{2}\lambda_{hs}v_0^2 \quad (2)$$

We restrict the parameters so that $m_s^2 > 0$, implying that $\langle s \rangle = 0$ in the true vacuum. The Higgs doublet components are

$$H = (\chi_1 + i\chi_2, h + i\chi_3)^T / \sqrt{2} \quad (3)$$

where h denotes the background Higgs field, and the χ 's are the Goldstone bosons.

The full effective potential takes into account one-loop corrections and temperature effects,

$$V_{\text{eff}} = V_0 + V_1 + V_{CT} + V_T \quad (4)$$

where V_0 is the tree-level potential (1), V_1 is the one-loop correction, V_{CT} contains the counterterms associated with V_1 , and V_T is the thermal contribution, including ring resummation of thermal masses. These expressions are standard, and we have described them in detail in appendix A. V_{eff} is determined by the measured SM parameters and the three new ones, that we henceforth take to be w_0 , λ_{hs} and the singlet mass m_s by trading λ_s for m_s through eq. (2).

III. PHASE TRANSITION

Because of our assumption that $\langle s \rangle = 0$ at low temperatures, the $\lambda_{hs}h^2s^2$ coupling creates a barrier in field space between the false and true vacua, and gives rise to a two-step phase transition. At temperatures $T \gg w$, the minimum of the potential is at the origin, where both electroweak symmetry and the Z_2 symmetry are restored. At some temperature T' , the first transition occurs, where $\langle s \rangle \rightarrow w'$ (see fig. 1). As T decreases, $\langle s \rangle$ and the corresponding minimum of the potential becomes metastable. At the critical temperature T_c , the two minima become degenerate, and at a slightly lower temperature T_n nucleation of bubbles begins, signaling the second transition where electroweak symmetry is broken while the Z_2 symmetry is restored. These two transitions are summarized as

1. At $T = T'$ (h, s) : $(0, 0) \rightarrow (0, w')$
2. At $T = T_n$ (h, s) : $(0, w_n) \rightarrow (v_n, 0)$.

It is the second transition that is important for baryogenesis. We note that while domain walls could

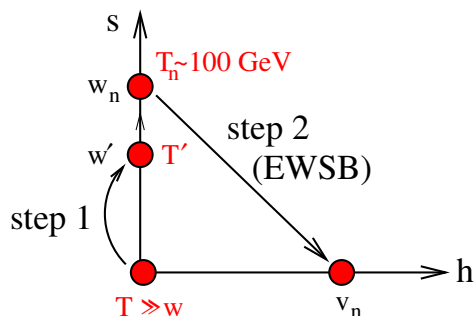


FIG. 1. Sequence of phase transitions in field space.

form during the first transition, the restoration of the Z_2 symmetry during the second transition will cause them to annihilate. This occurs long before they can dominate the energy density of the universe, hence we expect that no cosmological problems will arise from this brief appearance of domain walls [13].

The dynamics of the phase transition depend strongly on T_n , the temperature at which the probability of a bubble nucleating within one Hubble volume per Hubble time is $\mathcal{O}(1)$ [17]. The tunneling probability goes as $\exp(-S_3/T)$, where S_3 is the three-dimensional Euclidean action. We used CosmoTransitions [18] to find phase transition candidates and to determine T_n ¹. The criterion for the nucleation temperature is taken to be $S_3/T_n = 140$ [17].

Since our investigation is motivated by electroweak baryogenesis, we focus attention on first order transitions that are strong enough to preserve the baryon asymmetry from washout by residual sphaleron interaction inside the bubbles. This requires the Higgs VEV at the nucleation temperature to satisfy [19]

$$\frac{v_n}{T_n} \gtrsim 1.1. \quad (5)$$

IV. WALL DYNAMICS

The bubble-wall dynamics are determined by the interactions of the Higgs and singlet fields with a thermal fluid consisting of top quarks, electroweak gauge bosons, and any other particles to which the scalars couple significantly. After the bubble nucleates, it expands due to the outward pressure caused by the potential difference between the phases of the scalar fields on either side. The interactions of the wall with the surrounding fluid counteract the expansion by a friction force that depends on the speed and shape of the wall.

¹ CosmoTransitions occasionally fails to find transitions when they should exist; in such cases, changing the value of λ_{hs} by $\mathcal{O}(10^{-6})$ can overcome the problem. Moreover, CosmoTransitions often reports more phase transitions than expected for a given model; we find that defining the EWPT as the most recent first order transition where the Higgs' VEV in the unbroken phase is smaller than the nucleation temperature gives correct results. Of those, only phase transitions that ended with no singlet VEV were studied. We found it a useful cross-check to require the transition identified by CosmoTransitions to have a critical temperature that matched our own calculations for the parameter point in question.

If the friction is strong enough, the bubbles reach a steady-state velocity whose value is relevant for gravitational waves and baryogenesis. The terminal v_w depends upon the field profiles that solve the equations of motion. These in turn depend upon the temperature T_w of the wall and the v_w -dependent friction exerted by the plasma on the wall, leading to $T_w > T_n$, due to heating by the fluid. A self-consistent solution thus requires simultaneously solving for v_w and the scalar field profiles in the wall.

IV.1. Deflagration profiles

The wall temperature, and the rest of the dynamics of the bubble, depend on whether the phase transition proceeds through deflagrations or detonations (hybrids of these two are also possible). For subsonic bubble walls, with $v_w < 1/\sqrt{3}$, the bubbles grow via deflagrations [10], in which the wall is preceded by a shock front that moves through the fluid, perturbing it, increasing the temperature from T_n to T_s and causing the wall to move (see fig. 2). The fluid velocity decreases until the point where the wall passes it, so that the fluid behind the wall is at rest relative to that preceding the shock front. In this work we limit our investigation to the case of deflagrations, hence subsonic walls, deferring the study of supersonic walls to the future [20].

Because of the heating, the bubble wall dynamics are not determined at temperature T_n , but rather the temperature of the fluid near the wall. The calculation is performed at times sufficiently long after nucleation that the bubble has reached a steady-state velocity, and the profiles of the fluid perturbations vary on scales much larger than the wall thickness. Therefore one approximates the wall as a discontinuity, such that the fluid temperature is T_+ (T_-) just in front of (behind) the wall. The fluid velocity likewise is discontinuous there.

Since it is often convenient to switch between reference frames, we adopt the notation v_{xy} for the velocity of x in the reference frame y . In this context, x and y either refer to the wall (w), shock front (s), or the fluid at position 1 (in front of the wall), 2 (behind the shock front), or u (the unperturbed “universe” frame, in front of the shock front or behind the wall). The wall velocity, which is measured with respect to the fluid directly in front of the wall, is v_{w1} in this notation. We note that for any x and y , $v_{xy} = -v_{yx}$. A diagram depicting the geometry and labels is shown in fig. 2.

The relationships between the various fluid velocities and temperatures are found by integrating the stress tensor $T_{\mu\nu}$ across either of the two interfaces shown in fig. 2. Approximating the fluid as perfect,

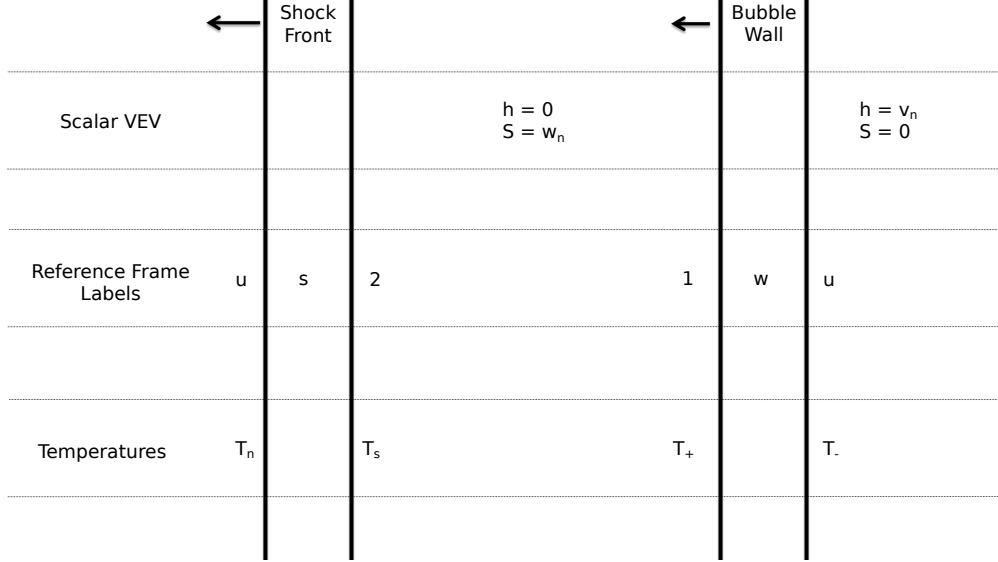


FIG. 2. Illustration of the geometry of a deflagration. The bubble wall and shock front are moving to the left with the inside of the bubble being on the right of the figure.

these depend only on the fluid density and pressure. The equations of state can be expressed as [16]

$$p_{\pm} = \frac{1}{3}a_{\pm}(T_n)T_{\pm}^4 - \epsilon_{\pm}(T_n) \quad (6)$$

$$\rho_{\pm} = a_{\pm}(T_n)T_{\pm}^4 + \epsilon_{\pm}(T_n) \quad (7)$$

where ρ_{\pm} is the fluid density on either side of the bubble wall and p_{\pm} is the pressure. a_{\pm} and ϵ_{\pm} are given by

$$a_{\pm}(T) = -\frac{3}{4T^3} \frac{d\mathcal{F}_{\pm}(T)}{dT} \quad (8)$$

$$\epsilon_{\pm}(T) = \mathcal{F}_{\pm}(T) + \frac{1}{3}a_{\pm}(T)T^4. \quad (9)$$

\mathcal{F}_{\pm} is the free energy of the fluid evaluated at the respective VEVs outside and inside wall and $T = T_n$. It is given by

$$\mathcal{F}(h, s, T) = V_{\text{eff}}(h, s, T) - \frac{g'_* \pi^2}{90} T^4. \quad (10)$$

Here $g'_* = 107.75 - 24.5 = 83.25$ is the effective number of degrees of freedom, apart from the t , W/Z , h , χ and s , whose contributions are already included in V_{eff} . In general, $a_{\pm}(T)$ and $\epsilon_{\pm}(T)$ in (6,7) should be evaluated at the temperatures T_{\pm} , but for transitions typically of interest for baryogenesis, where there is a limited degree of supercooling, the T -dependence of $a(T)$ and $\epsilon(T)$ is insignificant.

Integrating $T_{\mu\nu}$ across the bubble wall provides the relations [10]

$$v_{w1}v_{wu} = \frac{p_+ - p_-}{\rho_+ - \rho_-}, \quad \frac{v_{w1}}{v_{wu}} = \frac{p_+ + p_-}{\rho_+ + \rho_-}. \quad (11)$$

Integrating across the shock front, the temperature changes, but not the the field values, leading to

$$v_{su}v_{s2} = \frac{1}{3}, \quad \frac{v_{su}}{v_{s2}} = \frac{T_n^4 + 3T_s^4}{3T_n^4 + T_s^4}. \quad (12)$$

Fluid velocities in the wall and shock wave frame are related by Lorentz transforming to the u frame using

$$v_{2u} = \frac{v_{su} - v_{s2}}{1 - v_{su}v_{s2}}, \quad v_{1u} = \frac{v_{wu} - v_{w1}}{1 - v_{wu}v_{w1}}. \quad (13)$$

The relationship between the fluid velocity and temperature behind the shock front and in front of the wall can be approximated by linearizing the stress-energy equations with respect to small fluid velocities in the universe frame [11], to obtain

$$T_s = T_+ \exp \left[\frac{-2v_{u1}v_{wu}^2 \left(\frac{1}{v_{wu}} - \frac{1}{v_{su}} \right)}{1 - 3v_{wu}^2} \right] \quad (14)$$

$$v_{2u} = v_{1u} \left(\frac{v_{wu}}{v_{su}} \right)^2 \left(\frac{3v_{su}^2 - 1}{3v_{wu}^2 - 1} \right) \quad (15)$$

For a given guess of the wall velocity, $v_w \equiv v_{w1}$, and an associated nucleation temperature, eqs. (11-15) can be used to solve for the eight remaining variables: T_+ , T_- , T_s , v_{wu} , v_{su} , v_{1u} , v_{2u} , and v_{s2} . An example of the solution to these equations for sample set of parameters is shown in fig. 3.

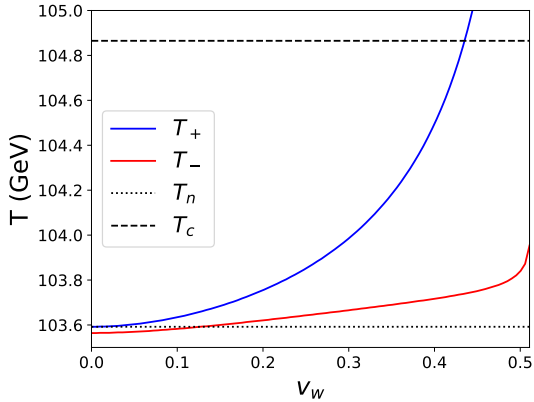


FIG. 3. An example of how the wall temperature changes as a function of v_w for a sample model with $m_s = 63$ GeV, $w_0 = 130$ GeV, and $\lambda_{hs} = 0.9$

IV.2. Equations of Motion

The equation of motion of a scalar field coupled to a perfect fluid has been derived by enforcing the conservation of the stress-energy tensor in the WKB approximation [7], or starting from the Kadanoff-Baym equations [15]. Both methods lead to

$$\square\phi + \frac{\partial V(\phi)}{d\phi} + \sum_i n_i \frac{dm_i^2}{d\phi} \int \frac{d^3p}{(2\pi)^3 2E} f_i(\vec{p}, x) = 0 \quad (16)$$

where $V(\phi)$ is the zero-temperature effective potential, the sum is over all particles that couple to ϕ , n_i is the number of degrees of freedom of particle i , m_i is its field-dependent mass, and $f_i(\vec{p}, x)$ is its phase space distribution. By separating $f_i = f_{0,i} + \delta f_i$ into equilibrium and out-of-equilibrium components, the equation of motion takes a more useful form. The integral over $f_{0,i}$ is equivalent to accounting for the T -dependence of the effective potential, giving

$$\square\phi + \frac{\partial V_{\text{eff}}(\phi, T)}{d\phi} + \sum_i n_i \frac{dm_i^2}{d\phi} \int \frac{d^3p}{(2\pi)^3 2E} \delta f_i(\vec{p}, x) = 0 \quad (17)$$

The third term in (17) describes the friction force that comes from the dissipative interactions between the scalar field and the surrounding fluid.

In the following, we assume that the dominant sources of friction are the top quark and electroweak gauge bosons. The lighter fermions, gluons and photons can be safely ignored because of their negligible couplings to the Higgs field. The self-couplings and mixing of the scalar fields are assumed to be subdominant due to their fewer degrees of freedom relative to vector bosons or quarks. It is possible that including these contributions would lead to moder-

ately slower walls, which could be advantageous for baryogenesis, but we defer this issue to future study.

For the electroweak phase transition considered here, there are two relevant scalar fields, each with its own equation of motion, that must be simultaneously solved. Eq. (17) can be further simplified by accounting for the spherical symmetry of the wall and going to the planar limit, which reduces the system to one spatial dimension, and by considering only the steady-state regime. Therefore, the equations of motion for a bubble wall traveling in the negative z direction become

$$-h''(z) + \frac{\partial V_{\text{eff}}(h, s, T)}{\partial h} \quad (18)$$

$$+ \sum_{i=t,W,Z} n_i \frac{dm_i^2}{dh} \int \frac{d^3p}{(2\pi)^3 2E} \delta f_i(\vec{p}, z) = 0$$

$$-s''(z) + \frac{\partial V_{\text{eff}}(h, s, T)}{\partial s} = 0 \quad (19)$$

where primes denote derivatives with respect to z . Strictly speaking, the existence of a steady-state solution to the equations of motion does not guarantee that those solutions will in fact be realized in the physical setting, but this issue is beyond the scope of this paper.

IV.3. Friction

The friction experienced by the wall depends on $\delta f_i(\vec{p}, z)$, the deviation from equilibrium of W/Z and t . We adopt the fluid approximation framework developed in [7], in which the friction is fully described by three fluids: that of the top quark, the massive gauge bosons, and the other particles, denoted as the “background.” We label the gauge boson contribution by W although it also includes Z . For simplicity W and Z are grouped together due to their similar couplings, and assigned a mass-squared that is the weighted average of m_W^2 and m_Z^2 . The background fluid encompasses all the fields that are assumed to contribute negligible friction, but which nevertheless play an important role in the wall dynamics. We consider friction only from fluid excitations with large momentum, such that the wavelength is shorter than the width of the wall. It has been shown that IR excitations in the massive gauge boson fluid can be important [21], but we have checked numerically that these are subdominant for parameters of interest in the present study, using the same approximations to evaluate the IR contributions as in ref. [16], but taking care to impose the perturbative cutoff $m_W(z) > g^2 T$ [21].

The phase space distribution for the t and W flu-

ids can be parametrized as

$$f_i(E, z) = \frac{1}{e^{(E+\delta_i(z))/T} \pm 1} \quad (20)$$

where the $+/-$ is for fermions/bosons and

$$\delta_i(z) = - \left[T(\delta\mu_i + \delta\mu_{bg})(z) + E(\delta\tau_i + \delta\tau_{bg})(z) + p_z(\delta v_i + \delta v_{bg})(z) \right] \quad (21)$$

accounts for perturbations in the fluids. $\delta\mu_i(z)$, $\delta\tau_i(z)$, $\delta v_i(z)$ are respectively the perturbations in the chemical potential, the relative temperature and the velocity. The subscript bg denotes the background fluid. All the perturbations are relative to the fluid directly in front of the wall where $\mu = 0$ and $T = T_+$ as described in section IV.1.

Deviations from equilibrium in the fluids are governed by the Boltzmann equation

$$\frac{d}{dt} f_i(E, z) = -C[f_i(E, z)]. \quad (22)$$

Rather than solving the full Boltzmann equation, one linearizes it in $\delta_i(z)$, and converts it to a system of ordinary differential equations by taking three moments: $\int d^3p/(2\pi)^3$, $\int (E/T) d^3p/(2\pi)^3$, and $\int p_z d^3p/(2\pi)^3$. A detailed derivation is provided in appendix B, leading to the coupled matrix equations

$$A_w(\vec{q}_w + \vec{q}_{bg})' + \Gamma_w \vec{q}_w = S_w \quad (23)$$

$$A_t(\vec{q}_t + \vec{q}_{bg})' + \Gamma_t \vec{q}_t = S_t \quad (24)$$

$$A_{bg} \vec{q}_{bg}' + \Gamma_{bg,w} \vec{q}_w + \Gamma_{bg,t} \vec{q}_t = 0 \quad (25)$$

where $\vec{q}_i^T = (\delta\mu_i, \delta\tau_i, \delta v_i)$. The A_i matrices for $i = W, t$ take the form

$$A_i \equiv \begin{bmatrix} v_w c_2^i & v_w c_3^i & \frac{1}{3} d_3^i \\ v_w c_3^i & v_w c_4^i & \frac{1}{3} d_4^i \\ \frac{1}{3} d_3^i & \frac{1}{3} d_4^i & \frac{1}{3} v_w d_4^i \end{bmatrix} \quad (26)$$

while the source terms are

$$S_i \equiv \frac{m'_i m_i}{T^2} \begin{bmatrix} v_w c_1^i \\ v_w c_2^i \\ 0 \end{bmatrix} \quad (27)$$

The coefficients c_j^i and d_j^i denote the integrals

$$c_j^i \left(\frac{m_i}{T} \right) \equiv \int \frac{d^3p}{(2\pi)^3} (-f'_{0,i}) \frac{E^{j-2}}{T^{j+1}} \quad (28)$$

and

$$d_j^i \left(\frac{m_i}{T} \right) \equiv \int \frac{d^3p}{(2\pi)^3} (-f'_{0,i}) \frac{p^2 E^{j-4}}{T^{j+1}} \quad (29)$$

where $f_{0,i}$ is the equilibrium distribution function for particle i . In previous literature (with the exception of ref. [22]), these coefficients were evaluated in the massless approximation, where $d_j^i = c_j^i$, setting $m_i/T = 0$. But for some phase transitions satisfying the sphaleron bound (5), $m_t/T > 1$ in the broken phase; hence we derived the full mass dependence for this work. For the background fluid, one can show that

$$A_{bg} = 20A_w|_{m=0} + 78A_t|_{m=0} \quad (30)$$

where the background fluids are approximated as massless [15].

The Γ_i matrices in eqs. (23, 24) quantify the interactions of the fluids. Γ_t and Γ_w take the form

$$\Gamma_i \equiv T \begin{bmatrix} \Gamma_{\mu 1i} & \Gamma_{\delta T 1i} & 0 \\ \Gamma_{\mu 2i} & \Gamma_{\delta T 2i} & 0 \\ 0 & 0 & \Gamma_{vi} \end{bmatrix} \quad (31)$$

where the matrix elements are numerical constants calculated in [7] to be²

$$\Gamma_w/T = \begin{bmatrix} 0.00521 & 0.01012 & 0 \\ 0.01012 & 0.03686 & 0 \\ 0 & 0 & 0.01614 \end{bmatrix} \\ \Gamma_t/T = \begin{bmatrix} 0.00899 & 0.01752 & 0 \\ 0.01752 & 0.06906 & 0 \\ 0 & 0 & 0.03499 \end{bmatrix} \quad (32)$$

Using energy-momentum conservation, the background fluid collision terms are given by

$$\Gamma_{bg,i} = -n_i \Gamma_i \quad (33)$$

where $n_t = 12$ and $n_w = 9$ are the number of degrees of freedom in the respective components.

The background fluid is assumed to be in chemical equilibrium, implying that $\delta\mu_{bg} = 0$. This assumption removes the top row of eq. (25). The remaining two rows determine $\delta\tau_{bg}$ and δv_{bg} in terms of q_w and q_t ,

$$\vec{q}'_{bg} = -A_{bg23}^{-1} (\Gamma_{bg,w} \vec{q}_w + \Gamma_{bg,t} \vec{q}_t) \quad (34)$$

where A_{bg23}^{-1} denotes the matrix where the bottom right block of A_{bg} is inverted and the rest of the matrix elements are zero.

Equations (23) and (24) can then be expressed in 6×6 matrix form, in the rest frame of the bubble wall,

$$A\vec{q}' + \Gamma\vec{q} = S \quad (35)$$

² As we were completing this work, an improved numerical evaluation of these collision rates was presented in ref. [22].

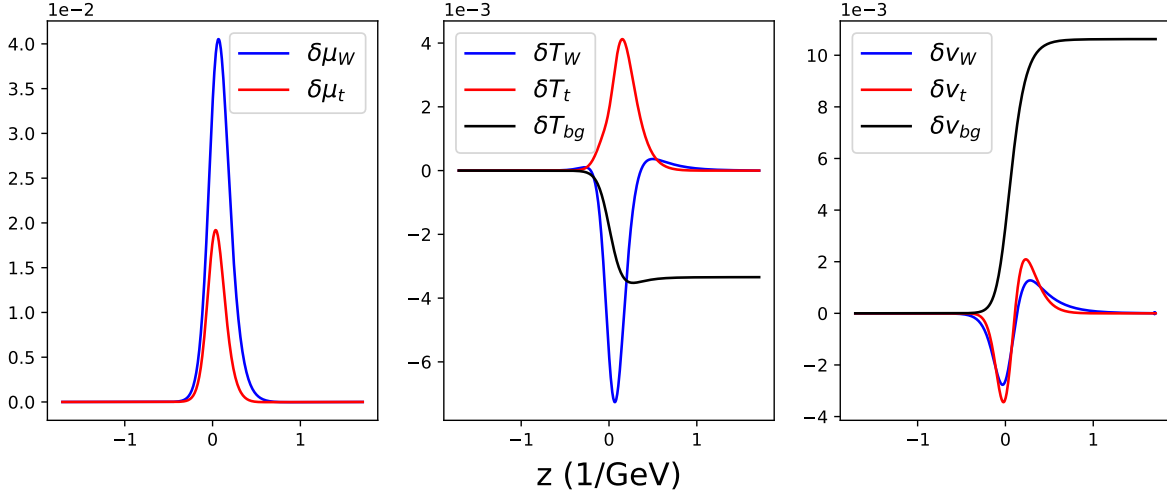


FIG. 4. Example of the solutions for the fluid perturbations, for a model with $m_s = 63$ GeV, $w_0 = 130$ GeV, and $\lambda_{hs} = 0.9$, $v_w = 0.297$ and background wall shape $h(z) = (h_0/2)[\tanh(z/L_w) + 1]$ where $h_0 = 209$ GeV and $L_w = 0.2$ GeV $^{-1}$.

with

$$A \equiv \gamma \begin{bmatrix} A_W & 0 \\ 0 & A_t \end{bmatrix}, \quad \vec{q} \equiv \begin{bmatrix} \vec{q}_w \\ \vec{q}_t \end{bmatrix}, \quad S \equiv \gamma \begin{bmatrix} S_w \\ S_t \end{bmatrix} \quad (36)$$

and

$$\Gamma \equiv \begin{bmatrix} \Gamma_w & 0 \\ 0 & \Gamma_t \end{bmatrix} - \begin{bmatrix} A_W A_{bg23}^{-1} \Gamma_{bg,w} & A_W A_{bg23}^{-1} \Gamma_{bg,t} \\ A_t A_{bg23}^{-1} \Gamma_{bg,w} & A_t A_{bg23}^{-1} \Gamma_{bg,t} \end{bmatrix} \quad (37)$$

The factors of $\gamma = 1/\sqrt{1-v_w^2}$ are from Lorentz boosting to the rest frame of the wall.

The W and t fluid perturbations are determined by solving eq. (35) using the relaxation method as described in ref. [23], since shooting tends to be unstable. The background fluid perturbations are found by integrating eq. (34). One can carry out this procedure for given values of the wall velocity and shape, and from the ensuing perturbations compute the friction term in the Higgs field equation of motion (18) using

$$\begin{aligned} \int \frac{d^3p}{(2\pi)^3 2E} \delta f_i(\vec{p}, z) &\cong \int \frac{d^3p}{(2\pi)^3 2E} f'_{0,i}(\vec{p}, z) \delta_i(z) \\ &= \frac{T^2}{2} \left[c_1^i(z) \delta \mu_i(z) + c_2^i(z) (\delta \tau_i(z) + \delta \tau_{bg}(z)) \right] \end{aligned} \quad (38)$$

An example of the solutions for the perturbations is shown in fig. 4.

IV.4. Solving the Equations of Motion

With the friction calculated in eq. (38), the equations of motion that must be solved to determine v_w

and the shape of the wall are

$$\begin{aligned} -h''(z) + \frac{\partial V_{\text{eff}}(h, s, T_+)}{\partial h} \\ + \frac{n_t T_+}{2} \frac{dm_t^2}{dh} [c_1^t \delta \mu_t + c_2^t (\delta \tau_t + \delta \tau_{bg})] \end{aligned} \quad (39)$$

$$+ \frac{n_W T_+}{2} \frac{dm_W^2}{dh} [c_1^W \delta \mu_W + c_2^W (\delta \tau_W + \delta \tau_{bg})] = 0$$

$$-s''(z) + \frac{\partial V_{\text{eff}}(h, s, T_+)}{\partial s} = 0. \quad (40)$$

Deep into the bubble interior, eq. (39) is not exactly satisfied once we adopt our approximation schemes for calculating the effective potential and

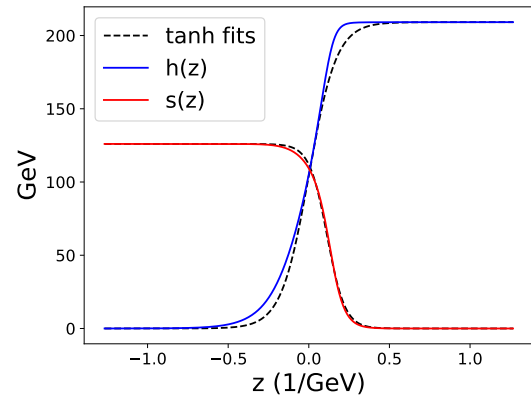


FIG. 5. The wall shape that solves the equation of motion for the model with $m_s = 63$ GeV, $w_0 = 130$ GeV, and $\lambda_{hs} = 0.9$. The dashed curves show the best fits using the tanh ansatz of eqs. (48, 49).

the perturbations. The Higgs' VEV is unchanging there, so the kinetic term is zero. Similarly the perturbations in the W and t fluids go to zero on both sides of the wall. This implies that the terms proportional to $\delta\tau_{bg}$ must exactly cancel out the potential term. When the perturbations are determined as described above and the potential term is calculated with the Higgs VEV that minimizes the potential inside the bubble, the two terms do not cancel as they should. This is due to differences in the derivation of the friction terms in comparison to the effective potential. Firstly, the fluid perturbations are only determined to linear order whereas the temperatures that go into the effective potential, T_+ and T_- , were calculated including non-linearities in the fluid equations. This means that while in theory $T_+ - T_- = T_+ \delta\tau_{bg}$, their relationship is only approximate. The other cause is that the scalar fields were treated as massless background fields in the friction calculation but their full contribution was included in the effective potential. There are three ways to account for this inconsistency: the Higgs VEV inside the bubble can be chosen not to minimize the potential but instead to cancel the friction term, the entire friction can be scaled to cancel the potential term but maintaining the friction shape in z , or just the background perturbation contribution to the friction can be scaled to cancel the potential term. We adopt the last option, which we found to be the most conservative choice (leading to slightly larger wall velocities). The equations of motion that we actually use to determine the wall dynamics then become

$$E_h \equiv -h''(z) + \frac{\partial V_{\text{eff}}(h, s, T_+)}{\partial h} \quad (41)$$

$$+ \frac{n_t T_+}{2} \frac{dm_t^2}{dh} [c_1^t \delta\mu_t + c_2^t (\delta\tau_t + y \delta\tau_{bg})] \\ + \frac{n_W T_+}{2} \frac{dm_W^2}{dh} [c_1^W \delta\mu_W + c_2^W (\delta\tau_W + y \delta\tau_{bg})] = 0$$

$$E_s \equiv -s''(z) + \frac{\partial V_{\text{eff}}(h, s, T_+)}{\partial s} = 0 \quad (42)$$

where y is an $\mathcal{O}(1)$ parameter chosen so that the equations are satisfied for larger positive values of z .

For a given value of v_w , the relaxation method can be used to find the shapes of $h(z)$ and $s(z)$ that come closest to solving the equations of motion. One must then vary v_w and find a complete solution to the equations, by iterating this procedure. A reasonable initial guess for both v_w and the wall shape is required, leading us to solve the equations in two stages. The first part is to guess v_w and the wall shape using the tanh ansatz employed in previous studies of wall velocities [7],[15],[16]. The second uses these as a starting point to numerically determine v_w and the wall shapes.

The tanh ansatz in the first stage assumes that the Higgs profile has the form

$$h(z) = \frac{v(T_-)}{2} \left(\tanh\left(\frac{z}{L_w}\right) + 1 \right) \quad (43)$$

where $v(T_-)$ is the Higgs VEV at temperature T_- and L_w is the width of the wall. The friction and shape of the singlet profile are independent of each other, so there is no need to impose a tanh ansatz for s ; rather its profile is found by numerically solving its equation of motion. This reduces the problem to finding values of v_w and L_w that come closest to solving the Higgs equation of motion³.

No choice of v_w and L_w will exactly solve eq. (41), since the true shape is not a tanh function. Instead we follow ref. [15] by calculating two moments of E_h in eq. (41) and finding the values of v_w and L_w that make them vanish. The two moments are taken to be

$$E_1 \equiv \int h'(z) E_h dz = 0 \quad (44)$$

$$E_2 \equiv \int h'(z) (2h(z) - v(T_-)) E_h dz = 0$$

since with this choice the Jacobian matrix $\partial(E_1, E_2)/\partial(v_w, L_w)$ is always far from being singular.

The first stage of the algorithm can then be summarized as:

1. Make a guess for v_w and L_w
2. Calculate T_+ and T_- for v_w
3. Determine $s(z)$ by solving the s equation of motion using the tanh ansatz for $h(z)$
4. Determine the shape of the friction term for the guessed shape of $h(z)$
5. Calculate the moments E_1 and E_2
6. Find the new guess for v_w and L_w by solving $E_i = 0$.

In the second stage, we aimed to relax the tanh profile assumption for $h(z)$ and to determine its shape more exactly. Using the values of v_w and L_w from the first part as new initial guesses, we solved both h and s equations of motion simultaneously,

³ In an alternative implementation of this initial stage, which is also effective, we fix the path through field space as an arc passing through the saddle point, and we work with the field equation along that path rather than giving priority to h or s .

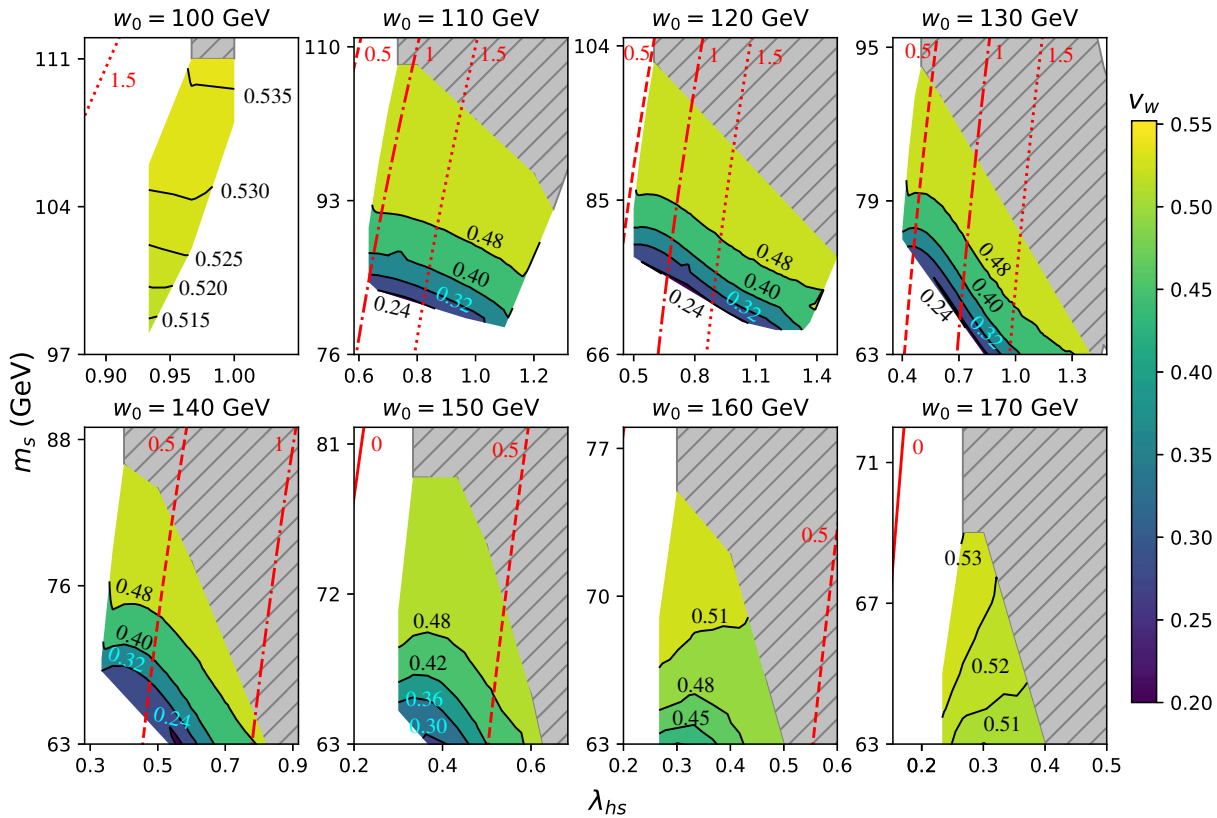


FIG. 6. Contours of the wall velocity v_w in the λ_{hs} - m_s plane, with w_0 increasing from 100 to 170 GeV in successive plots. The white area indicates regions where no first order transition satisfying the sphaleron bound (5) was found. In the grey hatched region, strong transitions satisfying (5) exist, but no solutions with $v_w < c_s$ were found. The red contours indicate values of the singlet self-coupling, λ_s , as determined by eq. (2). For each w_0 we show only regions containing viable solutions for the bubble wall parameters, within the ranges specified in Eqn. (46).

using relaxation. A challenge here is that the friction on the wall, which is expensive to compute, depends on the background $h(z)$ solution. To speed up the algorithm, we recomputed the friction only after several relaxation steps. This procedure leads to eventual convergence, unless the initial guess for v_w is too poor. Convergence was tested by seeing how closely the two equations of motion were satisfied, using the squared error statistic

$$E_{\text{tot}} = \int [E_h^2 + E_s^2] dz. \quad (45)$$

The best value of v_w was determined by varying v_w in the region of the guess from step 1 as to minimize E_{tot} . An example of the wall shapes that solve the equations of motion is given in fig. 5. It demonstrates that the actual profiles can differ significantly from the tanh ansatz.

V. RESULTS AND DISCUSSION

A scan of the parameter space of the scalar singlet model was performed in the ranges

$$\begin{aligned} 0.1 &\leq \lambda_{hs} \leq 1.5 \\ 63 \text{ GeV} &\leq m_s \leq 114 \text{ GeV}, \\ 100 \text{ GeV} &\leq w_0 \leq 170 \text{ GeV}. \end{aligned} \quad (46)$$

We did not find viable examples for $w_0 \lesssim 90$ or $\gtrsim 180$ GeV. Our results indicate that this covers most, if not all, of the parameter space of interest for subsonic walls.

We imposed the lower bound $m_s > m_h/2$ so that collider constraints from invisible Higgs decay ($h \rightarrow ss$) do not apply [24]. This is a mild restriction, since for $m_s < m_h/2$ and not too close to the upper limit, these constraints imply the invisible branching ratio is $\lesssim 25\%$, hence $\lambda_{hs} \lesssim 0.01$, which is too small to give rise to a strong phase transition.

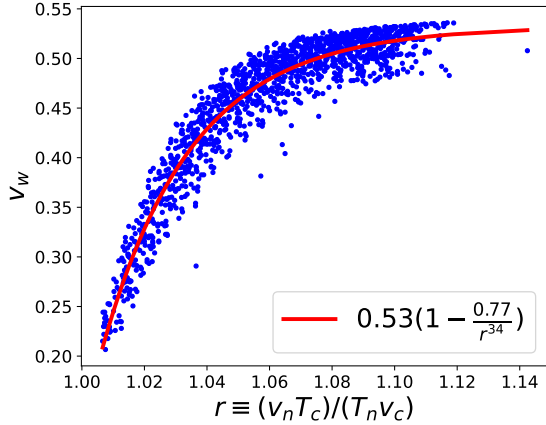


FIG. 7. The dependence of wall velocity, v_w , on the supercooling parameter, $r = (v_n/T_n)/(v_c/T_c)$. The solid curve shows a fit to the points.

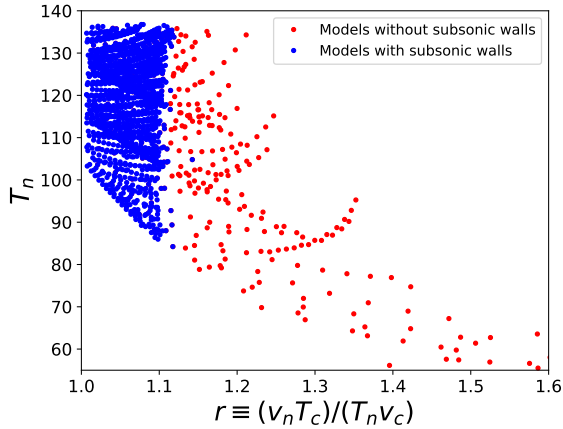


FIG. 8. Scatter plot of nucleation temperature T_n versus the supercooling parameter r , for all models CosmoTransitions found to satisfy the sphaleron washout condition.

V.1. Wall Velocity Results

Our determinations of the wall speed over the full parameter space are illustrated in in fig. 6, showing contours of v_w in the plane of m_s versus $\lambda_{h,s}$, for a series of w_0 values. The grey hatched regions indicate parameters for which no transitions with subsonic walls were found. One can see that models with heavier singlets and larger $\lambda_{h,s}$ couplings tend to produce faster-moving walls. Generally we find a minimum value for v_w , which depends on w_0 and is smallest for $w_0 \sim 120$ GeV, where the lowest speed $v_w \cong 0.22$ is found. The parameters specifying a few benchmark models and their resulting phase transition properties are shown in table I.

Since it is numerically expensive to compute v_w

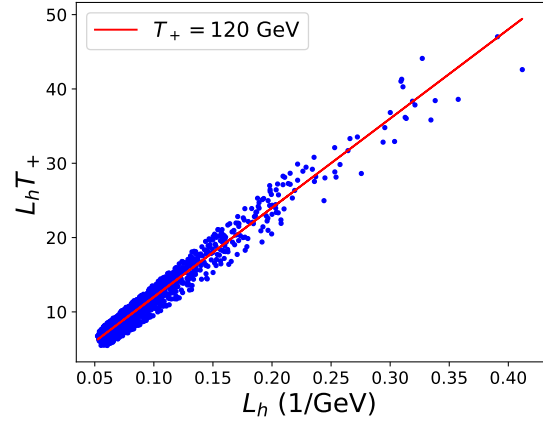


FIG. 9. The Higgs wall width L_h , in units of the inverse wall temperature T_+^{-1} , versus the same quantity in GeV^{-1} units. The solid line shows a fit to the points, corresponding to the mean wall temperature $T_+ = 120$ GeV.

for a given model from first principles, it is useful to look for relations between it and other quantities characterizing the strength of the phase transition, that are easier to compute. In fact we observe a strong correlation between v_w and the double ratio

$$r \equiv \frac{v_n/T_n}{v_c/T_c} \quad (47)$$

where v/T is evaluated respectively at the nucleation and the critical temperatures. This is a measure of the degree of supercooling, and its correlation with v_w is plotted in fig. 7, showing that v_w increases rapidly with $r - 1$. We find an analytic fit $v_w \cong 0.53(1 - 0.77r^{-34})$, with deviations of order ± 0.03 . The maximum value of r found for subsonic bubble walls was $r \cong 1.15$. It remains close to unity even for strong transitions, validating the assumption made in section IV.1 that the equations of state at the nucleation and critical temperatures do not differ significantly from each other.

The fact that a cutoff on r exists, above which it is unlikely to produce subsonic walls, can be seen in fig. 8, which shows all the models tested, including those

m_s	$\lambda_{h,s}$	w_0	v_w	T_n	T_c	v_n/T_n	r
63	0.9	130	0.297	103.592	104.865	2.02	1.02
81	1.0	110	0.336	124.301	125.425	1.40	1.03
66	0.3	160	0.492	130.532	132.677	1.28	1.05
105	0.8	110	0.530	130.646	134.461	1.24	1.11

TABLE I. Benchmark models with successively faster moving walls. Masses and temperatures are in GeV. r is the measure of supercooling defined in eq. (47).

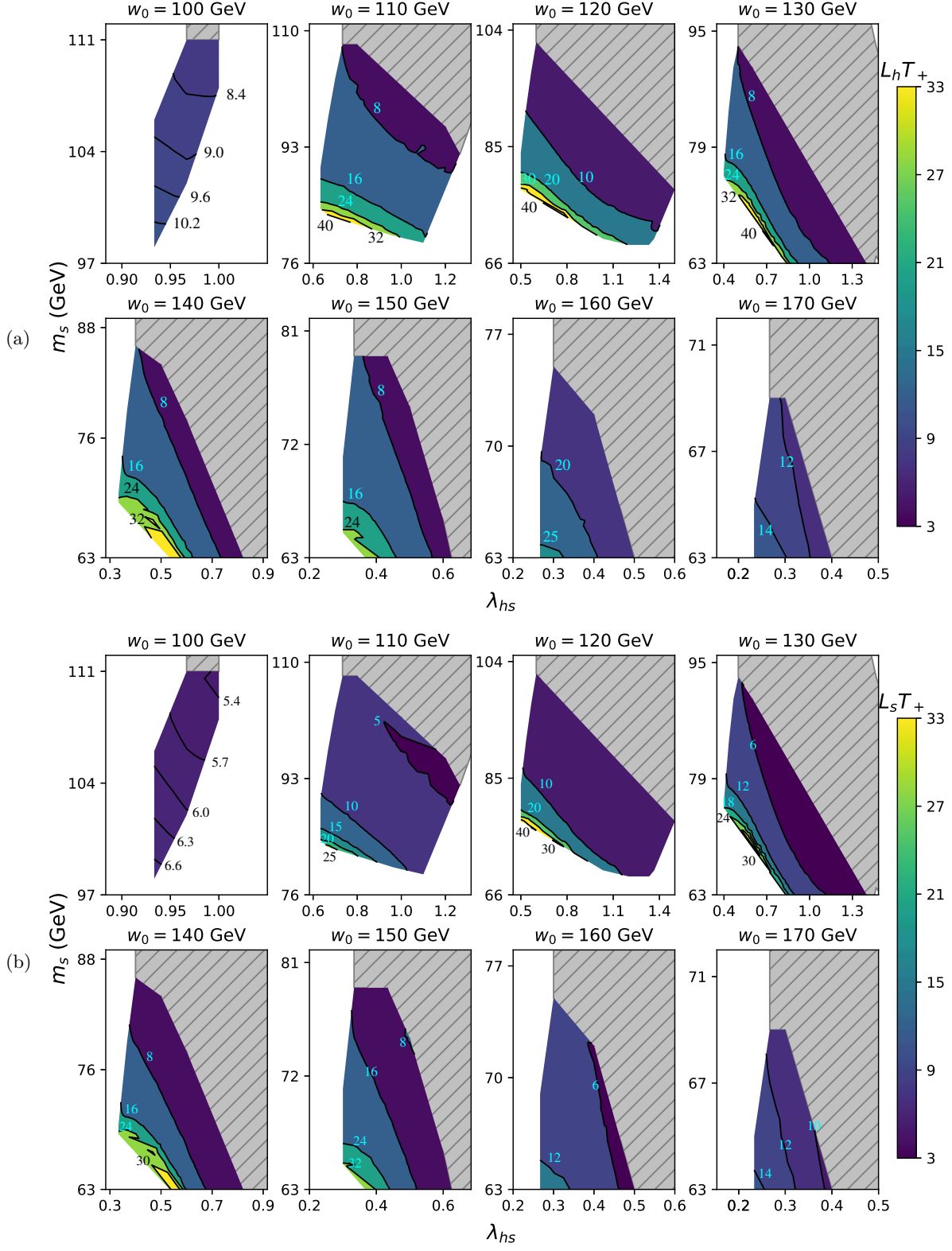


FIG. 10. Top two rows (a): Like fig. 6, but showing the contours of the Higgs wall width $L_h T_+$ where T_+ is the temperature in front of the bubble wall. Bottom two rows (b): Like fig. 6, but showing the contours of the singlet wall width $L_s T_+$.

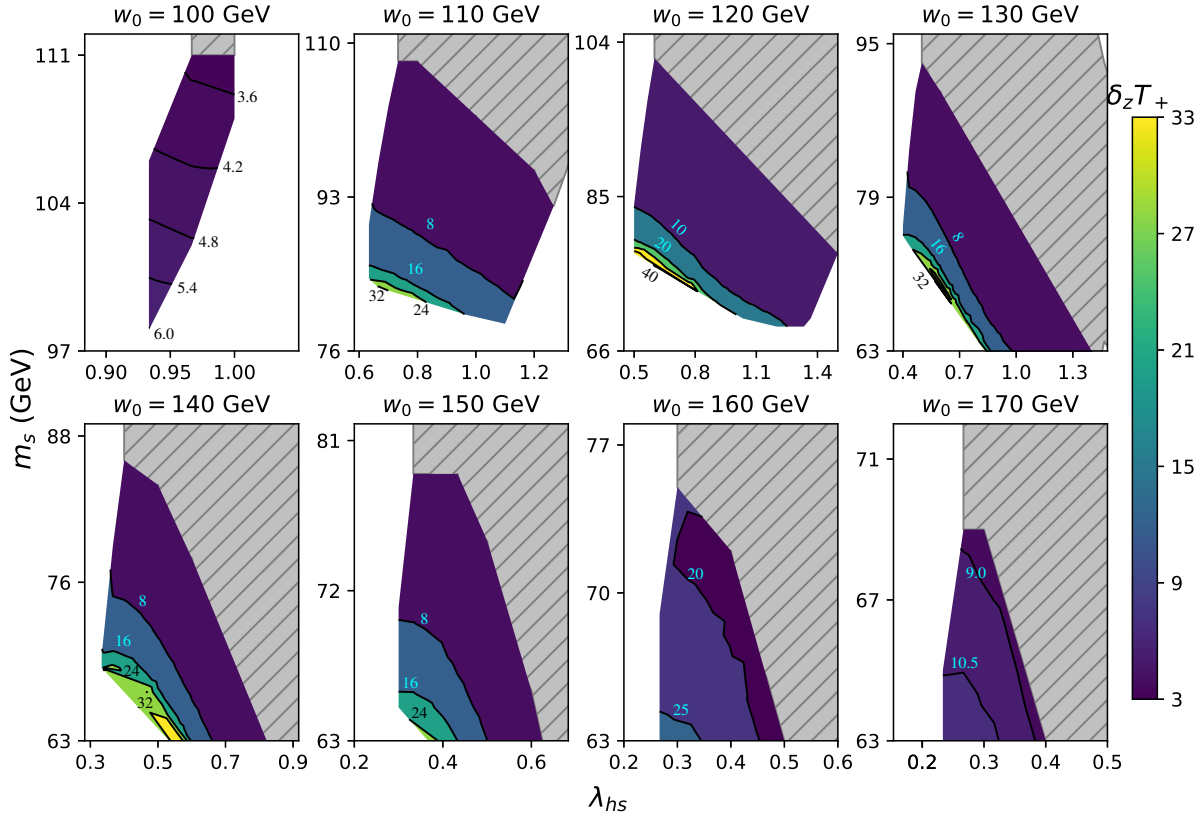


FIG. 11. Like fig. 6, but showing the contours of the wall separation parameter δ_z , defined in eq. (49).

found not to have slow bubble walls. It clearly shows that for $r \gtrsim 1.1$, few transitions produce subsonic walls, whereas below that point all the models tested were found to do so.

Fig. 6 shows that subsonic walls require the singlet to be relatively light, $m_s \lesssim 110$ GeV, often with a relatively large coupling to the Higgs, $\lambda_{hs} \sim 1$. If s is long-lived enough to escape detection within a collider, Ref. [25] suggests that a singlet with these properties may be a realistic target for the high-luminosity LHC (in the MET plus forward jets channel, from vector-boson fusion production of an off-shell Higgs). On the other hand, if we take the model at face value, as a complete model with a standard thermal history, Ref. [25] also finds that the LUX direct detection experiment [26] rules out $m_s \lesssim 120$ GeV even though s would make a subdominant contribution to the dark matter. Of course, additional model ingredients can easily make s unstable on cosmological time scales without affecting our phase-transition and wall-velocity results.

V.2. Wall Shape Results

Although Fig. 5 shows that the wall shapes deviate from a tanh profile, it is nevertheless a useful approximation for concisely encoding information about the wall shapes. We have accordingly analyzed our results from the fully numerical algorithm to find the best-fit tanh profiles, including a possible offset δ_z between the Higgs and the singlet profiles:

$$h_{\text{fit}} = \frac{h_0}{2} \left[1 + \tanh \left(\frac{z}{L_h} \right) \right] \quad (48)$$

$$s_{\text{fit}} = \frac{s_0}{2} \left[1 - \tanh \left(\frac{z - \delta_z}{L_s} \right) \right], \quad (49)$$

where we have allowed for independent widths L_h and L_s of the Higgs and singlet profiles.

To display results for the wall thicknesses, we have opted to use dimensionless combinations like $L_h T_+$, where T_+ is the temperature of the wall. If one wants to translate these into absolute thicknesses, it can be done using the strong correlation between $L_h T_+$ and L_h in GeV^{-1} units, shown in Fig. 9. Since all models with subsonic walls have nucleation temperatures in

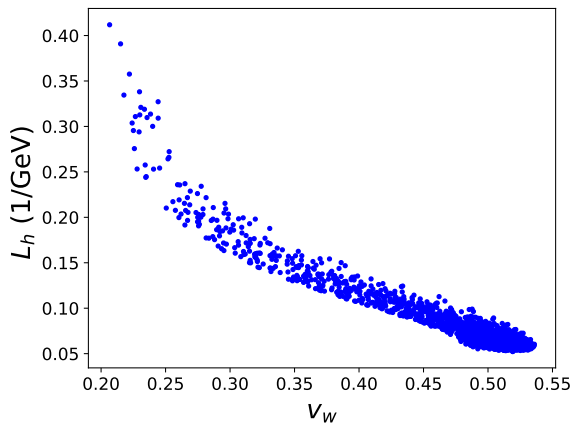


FIG. 12. The dependence of Higgs wall width, L_h , on the wall velocity, v_w .

the range $80 \text{ GeV} \leq T_n \leq 140 \text{ GeV}$ (see Fig. 8), and for slow walls the wall temperature does not deviate much from the nucleation temperature, the relationship between these two ways of characterizing L_h is linear with relatively little scatter: $L_h T_+ \cong L_h 120 \text{ GeV}$. This reflects the fact that the deviations of wall temperature from the mean value $T_+ = 120 \text{ GeV}$ are relatively small.

Contour plots of $L_h T_+$, $L_s T_+$, and $\delta_z T_+$ similar to those for v_w are presented in Figs. 10 and 11. We find that faster walls tend to be thinner and have smaller offsets. These relationships are plotted in Figs. 12-14, which show strong correlations, especially in the case of L_h . With rare exceptions, $L_s < L_h$, with L_s typically smaller than L_h by 20-30%.

As discussed in Appendix C, a small number of points were found to have extra potential minima or plateaus in the middle of the wall. The results for these points are likely to change with a more careful treatment of the effective potential. However, these points are rare, and including them does not change any of our conclusions.

VI. CONCLUSION

This work has laid out a more quantitative methodology than has been previously used, for calculating the wall velocity of bubbles during the electroweak phase transition with an additional scalar field. We improved on previous similar studies by solving for the actual profiles of the scalar fields, rather than just parametrizing them using a tanh ansatz. Other improvements made here include use of the one-loop Coleman-Weinberg contributions to the potential including the effect of thermal masses,

accounting for the sphericity of the bubbles, not expanding fluid perturbations to first order in m/T , and performing a scan over the three-dimensional parameter space.

Scanning over the parameter space reveals that the scalar singlet model is able to produce slow bubble walls that are preferable for electroweak baryogenesis to occur, down to a minimum wall velocity of $v_w \cong 0.22$. These examples of slow-moving walls only occur in phase transitions with small amounts of supercooling.

There are a few ways in which this study can be extended by future work. The precision of the wall velocity calculation could be improved by including additional sources of friction such as from the scalar fields and IR gauge boson modes. For a complete analysis of electroweak baryogenesis in the Z_2 scalar singlet model, this analysis could be embedded in a more complete model that includes a new source of CP-violation in order to determine the size of the

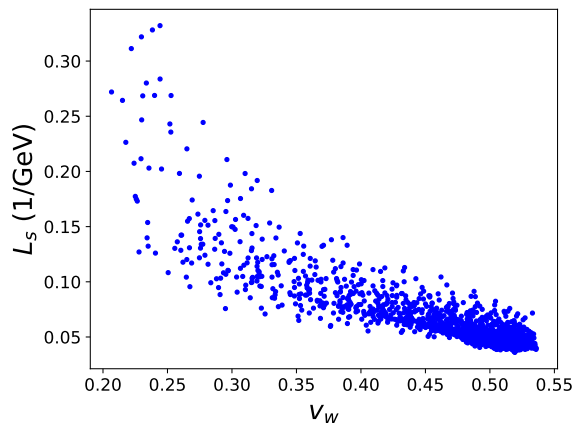


FIG. 13. Like fig. 12 but for L_s .

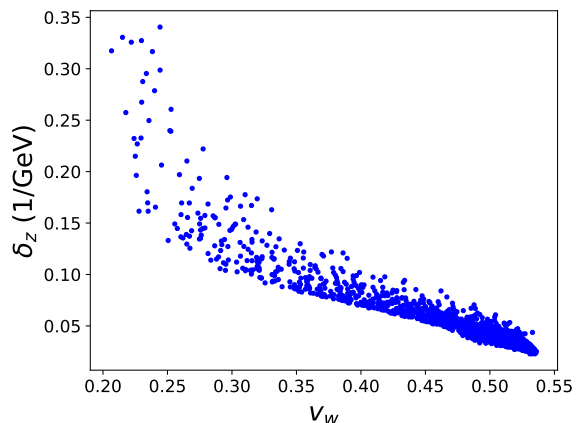


FIG. 14. Like fig. 12 but for δ_z .

matter anti-matter asymmetry that would be produced. Lastly, extending this analysis to apply for faster walls or even supersonic walls could be of interest for studying other effects of the phase transition such as gravitational waves. We are currently studying these issues [20].

ACKNOWLEDGMENTS

We thank B. Laurent for useful discussions and comments on the draft. JC and DTS thank the Aspen Center for Physics for providing a stimulating environment where this work was initiated. The computations in this work were run using equipment funded by the Canada Foundation for Innovation and supported by the Centre for Advanced Computing at Queen's University. Besides the previously mentioned CosmoTransitions, the code used for the calculations utilised Eigen [27] and the GNU Scientific Library [28]. AF and JC are supported by NSERC (Natural Sciences and Engineering Research Council, Canada).

Appendix A: Effective potential

The one-loop contribution to the potential can be approximated as

$$V_1 = \sum_{i=h,s,\chi,t,W,Z,\gamma} \frac{n_i m_i^4(h,s,T)}{64\pi^2} \left[\ln \left(\frac{m_i^2(h,s,T)}{v_0^2} \right) - c_i \right] \quad (\text{A1})$$

where n_i is the number of degrees of freedom of each particle. For the scalar fields, longitudinal W/Z and top quark $c_i = 3/2$ but for the transverse gauge bosons $c_i = 1/2$, in the $\overline{\text{MS}}$ scheme. The top quark is the only fermion included in the sum since the contributions from lighter fermions are suppressed by their small Yukawa couplings. χ stands for the Goldstone boson contributions.

The one-loop contribution acquires a temperature dependence through the thermal masses of the particles, in this method of carrying out the ring resummation [29]. It has been shown that for sufficiently strong phase transitions, a more careful treatment of thermal masses can be important [30].

The scalar masses in eq. (A1) are given by the eigenvalues of the mass matrix:

$$M_{\text{scalar},ij}^2 \equiv \frac{\partial^2 V}{\partial \phi_i \partial \phi_j} + m_{T,i}^2 \delta_{ij} \quad (\text{A2})$$

where ϕ_i and ϕ_j are the five scalar fields summed

over in eq. (A1) and

$$m_{T,h}^2 = T^2 \left(\frac{3g^2 + g'^2}{16} + \frac{y_t^2}{4} + \frac{\lambda_h}{2} + \frac{\lambda_{hs}}{24} \right) \quad (\text{A3})$$

$$m_{T,\chi}^2 = m_{T,h}^2 \quad (\text{A4})$$

$$m_{T,s}^2 = T^2 \left(\frac{\lambda_{hs}}{6} + \frac{\lambda_s}{4} \right). \quad (\text{A5})$$

The three mass eigenvalues associated with the Goldstone bosons vanish in the vacuum state making those terms in eq. (A1) formally divergent. This is properly dealt with by introducing a scale coinciding with the Higgs mass, m_h , to cut off the IR divergence [31].

The masses associated with the longitudinal modes of the gauge bosons in eq. (A1) are given by the eigenvalues of the mass matrix:

$$M_{\text{long},ij}^2 \equiv \begin{bmatrix} \frac{g^2 h^2}{4} & 0 & 0 & 0 \\ 0 & \frac{g'^2 h^2}{4} & 0 & 0 \\ 0 & 0 & \frac{g^2 h^2}{4} & \frac{gg' h^2}{4} \\ 0 & 0 & \frac{gg' h^2}{4} & \frac{g'^2 h^2}{4} \end{bmatrix} + \frac{11}{6} T^2 \text{diag}(g^2, g^2, g^2, g'^2) \quad (\text{A6})$$

The rest of the field-dependent masses in eq. (A1) are given by:

$$\begin{aligned} m_{\text{trans},w}^2 &= \frac{g^2 h^2}{4} \\ m_{\text{trans},z}^2 &= \frac{(g^2 + g'^2) h^2}{4} \\ m_{\text{trans},\gamma}^2 &= 0 \\ m_t^2 &= \frac{y_t^2 h^2}{2} \end{aligned} \quad (\text{A7})$$

The counterterm contribution to the potential can be parameterized as

$$V_{CT} = \frac{1}{2} \delta m_h^2 h^2 + \frac{1}{2} \delta m_s^2 s^2 + \frac{1}{4} \delta \lambda_h h^4 + \frac{1}{4} \delta \lambda_s s^4 + \frac{1}{4} \delta \lambda_{hs} h^2 s^2 \quad (\text{A8})$$

The five counterterms were chosen to ensure that the full effective potential at $T = 0$ maintains its tree-level values for the scalar masses, potential minima, and scalar mixing. This is done by imposing the following conditions at $T = 0$:

$$\left. \frac{\partial V}{\partial h} \right|_{h=v_0, s=0} = \left. \frac{\partial V}{\partial s} \right|_{h=0, s=w_0} = 0 \quad (\text{A9})$$

$$\left. \frac{\partial^2 V}{\partial h^2} \right|_{h=v_0, s=0} = m_h^2, \quad \left. \frac{\partial^2 V}{\partial s^2} \right|_{h=v_0, s=0} = m_s^2 \quad (\text{A10})$$

and

$$\left. \frac{\partial^4 V}{\partial h^2 \partial s^2} \right|_{h=v_0, s=0} = \lambda_{hs} \quad (\text{A11})$$

where $m_s = \sqrt{\frac{1}{2}\lambda_{hs}v_0^2 - \lambda_s w_0^2}$ is the mass of the scalar singlet in the true vacuum.

The resulting counterterm parameters are found to be

$$\delta m_h^2 = \left(\frac{1}{2} \frac{\partial^2 V_1}{\partial h^2} - \frac{3}{2v_0} \frac{\partial V_1}{\partial h} \right) \Big|_{h=v_0, s=0} \quad (\text{A12})$$

$$\delta m_s^2 = \left(-\frac{\partial^2 V_1}{\partial s^2} + \frac{v_0^2}{2} \frac{\partial^4 V_1}{\partial h^2 \partial s^2} \right) \Big|_{h=v_0, s=0} \quad (\text{A13})$$

$$\delta \lambda_h = \frac{1}{2v_0^2} \left(\frac{1}{v_0} \frac{\partial V_1}{\partial h} - \frac{\partial^2 V_1}{\partial h^2} \right) \Big|_{h=v_0, s=0} \quad (\text{A14})$$

$$\delta \lambda_s = -\frac{\delta m_s^2}{w_0^2} - \frac{1}{w_0^3} \frac{\partial V_1}{\partial s} \Big|_{h=0, s=w_0} \quad (\text{A15})$$

and

$$\delta \lambda_{hs} = -\frac{\partial^4 V_1}{\partial h^2 \partial s^2} \Big|_{h=v_0, s=0} \quad (\text{A16})$$

Lastly, the temperature dependence of the potential is given by

$$V_T = -\frac{12T^4}{2\pi^2} J_F \left(\frac{m_t(h)}{T} \right) + \sum_{i=h, s, \chi, W, Z} \frac{n_i T^4}{2\pi^2} J_B \left(\frac{m_i^2(h, s, T)}{T^2} \right) \quad (\text{A17})$$

where J_F and J_B are functions which describe fermions and bosons temperature-dependent contribution to the one-loop potential. The functions are calculated from

$$J_F(y) = \int_0^\infty x^2 \ln \left(1 + e^{-\sqrt{x^2 + y^2}} \right) dx \quad (\text{A18})$$

and

$$J_B(y) = \int_0^\infty x^2 \ln \left(1 - e^{-\sqrt{x^2 + y^2}} \right) dx \quad (\text{A19})$$

These equations fully describe the one-loop potential of the scalar fields.

Appendix B: Linearized Boltzmann Equations

The following derivation of the linearized moments to the Boltzmann equation, which are used to determine the friction of the equation of motion, follows closely to that originally expressed in [7]. The difference between that derivation and the one here is that the full dependence of m/T is included here instead of expanding to lowest order. This allows for stronger phase transitions to be quantitatively studied.

As noted in eqs. (20-22) the fluids are described by the distribution function

$$f_i(E, z) = \frac{1}{e^{E+\delta_i(z))/T} \pm 1} \quad (\text{B1})$$

where the $+/-$ is for fermions/bosons and

$$\delta_i(z) = -\left[T(\delta\mu_i + \delta\mu_{bg})(z) + E(\delta\tau_i + \delta\tau_{bg})(z) + p_z(\delta v_i + \delta v_{bg})(z) \right] \quad (\text{B2})$$

The background fluid is in chemical equilibrium so for the rest of the derivation $\delta\mu_{bg} = 0$. Deviations from equilibrium in the fluids are governed by the Boltzmann equation

$$\frac{df_i}{dt} = -C[f_i(E, z)] \quad (\text{B3})$$

The left side of eq. (B3) can be expanded as

$$\frac{df_i}{dt} = f'_{0,i} \left(\frac{dE}{dt} + \frac{d\delta_i}{dt} \right) \quad (\text{B4})$$

where

$$f'_{0,i} \equiv \partial_E f_i|_{\delta_i=0} \quad (\text{B5})$$

In the fluid's reference frame

$$\frac{d\delta_i}{dt} = \partial_t \delta_i + \frac{p_z}{E} \partial_z \delta_i - \frac{(m_i^2)'}{2E} \partial_{p_z} \delta_i \quad (\text{B6})$$

Starting with the last term

$$-\frac{(m_i^2)'}{2E} \partial_{p_z} \delta_i = \frac{(m_i^2)'}{2E} (\delta v_i + \delta v_{bg}) \quad (\text{B7})$$

As will be shown the perturbations are sourced by a term proportional to $\frac{(m_i^2)'}{2E} f'_{0,i}$ so terms like the one above which are proportional to $\frac{(m_i^2)'}{2E} f'_{0,i} \delta_i$ are on the same order as δ_i^2 and therefore are ignored to linear order.

This may raise the concern that if m_i/T is not small and $\delta_i \propto \frac{(m_i^2)'}{2E}$, does the linear approximation break down? The tanh ansatz can be used to

set a rough condition on the relation between v_n/T_n and LT under which taking the linear order is valid. That will be derived at the end of this section.

Next one observes that $\partial_t = v_w \partial_z$ in the fluid's reference frame, so to linear order in the perturbations

$$\frac{d\delta_i}{dt} = \left(v_w + \frac{p_z}{E}\right) \partial_z \delta_i. \quad (\text{B8})$$

Going back to eq. (B4), the term independent of δ_i acts as the source term in the perturbations equations.

$$\begin{aligned} \frac{dE}{dt} &= \frac{d}{dt}(p^2 + m_i^2)^{1/2} \\ &= \frac{1}{2(p^2 + m_i^2)^{1/2}} \frac{dm_i^2}{dt} \\ &= v_w \frac{(m_i^2)'}{2E} \end{aligned} \quad (\text{B9})$$

Therefore the Boltzmann equation becomes

$$f'_{0,i} \left(v_w + \frac{p_z}{E}\right) \partial_z \delta_i + C[f_i] = -v_w f'_{0,i} \frac{(m_i^2)'}{2E} \quad (\text{B10})$$

which when expanding out δ_i it becomes

$$\begin{aligned} -f'_{0,i} \left(v_w + \frac{p_z}{E}\right) [T\delta\mu'_i + E(\delta\tau'_i + \delta\tau'_{bg}) + p_z(\delta v'_i + \delta v'_{bg})] \\ + C[f_i] = -v_w f'_{0,i} \frac{(m_i^2)'}{2E} \end{aligned} \quad (\text{B11})$$

Three moments are taken to turn this into a system of ordinary differential equations. The three moments are $\int \frac{d^3p}{(2\pi)^3}$, $\int \frac{E}{T} \frac{d^3p}{(2\pi)^3}$, and $\int p_z \frac{d^3p}{(2\pi)^3}$.

When taking the first moment, all terms proportional to p_z integrate to zero leaving

$$\begin{aligned} \int \frac{d^3p}{(2\pi)^3} \left(-f'_{0,i} v_w [T\delta\mu'_i + E(\delta\tau'_i + \delta\tau'_{bg})] \right. \\ \left. - f'_{0,i} \frac{p_z^2}{E} (\delta v'_i + \delta v'_{bg}) + C[f_i] \right) \\ = \int \frac{d^3p}{(2\pi)^3} \left(-v_w f'_{0,i} \frac{(m_i^2)'}{2E} \right) \end{aligned} \quad (\text{B12})$$

Two sets of variables are then introduced.

$$c_j^i = - \int f'_{0,i} \frac{E^{j-2}}{T^{j+1}} \frac{d^3p}{(2\pi)^3} \quad (\text{B13})$$

and

$$d_j^i = - \int f'_{0,i} \frac{p^2 E^{j-4}}{T^{j+1}} \frac{d^3p}{(2\pi)^3} \quad (\text{B14})$$

After noting that $p_z^2 = p^2/3$ and substituting eqs. (B13, B14) into eq. (B12), one gets

$$\begin{aligned} T^4 v_w c_2^i \delta\mu'_i + T^4 v_w c_3^i (\delta\tau'_i + \delta\tau'_{bg}) \\ + T^4 v_w d_3^i (\delta v'_i + \delta v'_{bg})/3 + \int \frac{d^3p}{(2\pi)^3} C[f_i] \\ = \frac{T^2 v_w c_1^i (m_i^2)'}{2} \end{aligned} \quad (\text{B15})$$

or after factoring out the T^4

$$\begin{aligned} v_w c_2^i \delta\mu'_i + v_w c_3^i (\delta\tau'_i + \delta\tau'_{bg}) \\ + v_w d_3^i (\delta v'_i + \delta v'_{bg})/3 + \int \frac{d^3p}{(2\pi)^3} \frac{C[f_i]}{T^4} \\ = \frac{v_w c_1^i (m_i^2)'}{2T^2} \end{aligned} \quad (\text{B16})$$

The second moment equation is the exact same except with an extra factor of E/T in each term leading to

$$\begin{aligned} v_w c_3^i \delta\mu'_i + v_w c_4^i (\delta\tau'_i + \delta\tau'_{bg}) \\ + v_w d_4^i (\delta v'_i + \delta v'_{bg})/3 + \int \frac{d^3p}{(2\pi)^3} \frac{E C[f_i]}{T^5} \\ = \frac{v_w c_2^i (m_i^2)'}{2T^2} \end{aligned} \quad (\text{B17})$$

For the third moment equation, due to the extra factor of p_z , the opposite set of terms in eq. (B11) compared to the first two moments integrates to zero leaving

$$\begin{aligned} \int \frac{d^3p}{(2\pi)^3} \left(-f'_{0,i} \frac{p_z^2}{E} [T\delta\mu'_i + E(\delta\tau'_i + \delta\tau'_{bg})] \right. \\ \left. - f'_{0,i} v_w p_z^2 (\delta v'_i + \delta v'_{bg}) \right) = 0 \end{aligned} \quad (\text{B18})$$

which becomes

$$\begin{aligned} d_3^i \delta\mu'_i/3 + d_4^i (\delta\tau' + \delta\tau'_{bg})/3 \\ + v_w d_4^i (\delta v'_i + \delta v'_{bg})/3 = 0 \end{aligned} \quad (\text{B19})$$

As originally stated in section IV, eqs. (B16, B17, and B19) form a linear system of ODE's that takes the form

$$A_i(\vec{q}_i + \vec{q}_{bg})' + \Gamma_i \vec{q}_i = S_i \quad (\text{B20})$$

with A_i , Γ_i , S_i , and q_i all taking the same form as they do in section IV.

Perturbations, q_i , are sourced by a term proportional to $\frac{(m_i^2)'}{2T^2}$ so if $\frac{(m_i^2)'}{2T^2} \sim 1$ treating perturbations to linear order is no longer valid. To determine a rough quantitative condition of when this is true the tanh ansatz can be used where the Higgs wall shape is

$$h(z) = \frac{v}{2} \left(\tanh\left(\frac{z}{LT}\right) + 1 \right) \quad (\text{B21})$$

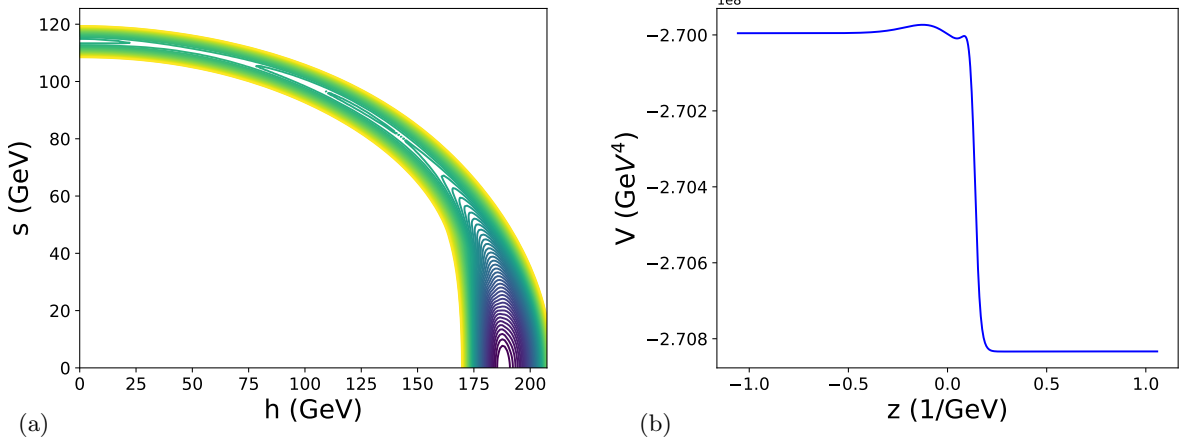


FIG. 15. Left (a): Contours of V_{eff} for the model with $\lambda_{hs} = 1.2$, $w_0 = 120$ GeV, and $m_s = 69$ GeV, evaluated at the wall temperature of $T_+ = 114.075$ GeV. Right (b): The potential for this model projected on the shape of the wall.

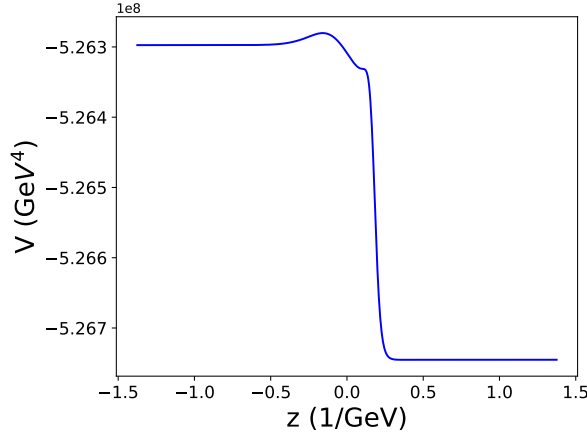


FIG. 16. The scalar potential along the wall for the model with $\lambda_{hs} = 0.9$, $w_0 = 110$ GeV, and $m_s = 81$ GeV evaluated at the wall temperature of $T_+ = 126.130$ GeV.

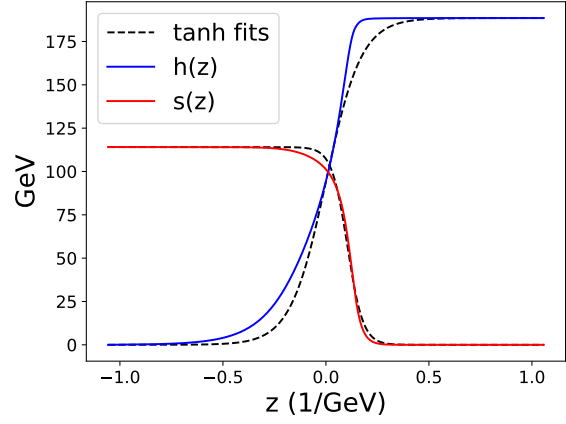


FIG. 17. The shape of the scalar fields for the model with $\lambda_{hs} = 1.2$, $w_0 = 120$ GeV, and $m_s = 69$ GeV.

This conditions will first break down with the top quark which has a mass given by

$$m_t(z)/T = \frac{y_t h(z)}{\sqrt{2}T} \quad (\text{B22})$$

Then by taking the derivative

$$\frac{(m_t^2)'}{2T^2} = \frac{(\frac{v}{T})^2 y_t^2 \text{sech}^2(\frac{z}{LT}) \left(\tanh(\frac{z}{LT}) + 1 \right)}{8LT} \quad (\text{B23})$$

At its maximum value this is equal to

$$\frac{(m_t^2)'}{2T^2} \Big|_{\text{max}} = \frac{4(\frac{v}{T})^2 y_t^2}{27LT} \quad (\text{B24})$$

By ensuring that $\frac{(m_t^2)'}{2T^2} \Big|_{\text{max}} < 1$ we get the condition

$$\left(\frac{v}{T} \right)^2 < 6.9 LT \quad (\text{B25})$$

This condition is easily met by all the wall found to have subsonic walls in this paper therefore indicating that the linear order approximation is valid.

Appendix C: Questionable Transitions

Some of the models included in this analysis have features in their potential that are likely to be sensitive to higher-order corrections. The two types of features seen are additional local minima and

plateaus in the potential in the middle of the bubble wall. An example of a model with such a minimum can be seen in fig. 15 which shows a potential with an additional local minimum in the h - s plane and spatially along the wall respectively. Similarly, an example of a wall profile with a potential plateau can be seen in fig. 16. These features appear in the potential when the bosonic squared masses become negative. This phenomenon, was first discussed in [31], where it was pointed out that this is sensitive to IR corrections to the potential. Including the thermal masses in the one-loop calculation of the effective potential reduced the frequency that models with these features appear. Due to the fact they are sensitive to IR corrections, these models are more likely to change from a more complete treatments of thermal resummation as discussed in [30] and including higher order loops in the effective potential. While that may make these specific models less robust, removing them does not change any of the trends or conclusions discussed in this paper and therefore even if more complete calculations change these models, the overall results should hold. Sam-

ple benchmark models that have these features are summarised in table II.

m_s	λ_{hs}	w_0	T_n	T_+	v_w	Feature Type
81	0.9	110	125.971	126.130	0.265	Plateau
80	0.967	110	125.139	125.302	0.267	Minimum
69	1.2	120	113.811	114.075	0.295	Minimum

TABLE II. Models which were found to have extra local minima or plateaus in the scalar potential evaluated at $T = T_+$. Masses and temperatures are all reported in GeV.

A final observation relating to these points is that they tend to have lower wall velocities and shapes that deviate more strongly from a tanh profile, as seen in fig. 17. If these minima are indeed physical, or if another physics model can produce similar physical effects, then removing the tanh ansatz is even more important for capturing the true wall behaviour.

-
- [1] K. Kajantie, M. Laine, K. Rummukainen, and M. E. Shaposhnikov, “A Nonperturbative analysis of the finite T phase transition in $SU(2) \times U(1)$ electroweak theory,” *Nucl. Phys.* **B493** (1997) 413–438, [arXiv:hep-lat/9612006](#) [hep-lat].
- [2] K. Kajantie, M. Laine, K. Rummukainen, and M. E. Shaposhnikov, “Is there a hot electroweak phase transition at $m(H)$ larger or equal to $m(W)$?,” *Phys. Rev. Lett.* **77** (1996) 2887–2890, [arXiv:hep-ph/9605288](#) [hep-ph].
- [3] D. E. Morrissey and M. J. Ramsey-Musolf, “Electroweak baryogenesis,” *New J. Phys.* **14** (2012) 125003, [arXiv:1206.2942](#) [hep-ph].
- [4] C. Caprini *et al.*, “Detecting gravitational waves from cosmological phase transitions with LISA: an update,” *JCAP* **03** (2020) 024, [arXiv:1910.13125](#) [astro-ph.CO].
- [5] B.-H. Liu, L. D. McLerran, and N. Turok, “Bubble nucleation and growth at a baryon number producing electroweak phase transition,” *Phys. Rev.* **D46** (1992) 2668–2688.
- [6] G. D. Moore and T. Prokopec, “Bubble wall velocity in a first order electroweak phase transition,” *Phys. Rev. Lett.* **75** (1995) 777–780, [arXiv:hep-ph/9503296](#) [hep-ph].
- [7] G. D. Moore and T. Prokopec, “How fast can the wall move? A Study of the electroweak phase transition dynamics,” *Phys. Rev.* **D52** (1995) 7182–7204, [arXiv:hep-ph/9506475](#) [hep-ph].
- [8] P. John and M. G. Schmidt, “Do stops slow down electroweak bubble walls?,” *Nucl. Phys.* **B598** (2001) 291–305, [arXiv:hep-ph/0002050](#) [hep-ph].
- [Erratum: *Nucl. Phys.*B648,449(2003)].
- [9] S. J. Huber and M. Sopena, “The bubble wall velocity in the minimal supersymmetric light stop scenario,” *Phys. Rev.* **D85** (2012) 103507, [arXiv:1112.1888](#) [hep-ph].
- [10] J. R. Espinosa, T. Konstandin, J. M. No, and G. Servant, “Energy Budget of Cosmological First-order Phase Transitions,” *JCAP* **1006** (2010) 028, [arXiv:1004.4187](#) [hep-ph].
- [11] S. J. Huber and M. Sopena, “An efficient approach to electroweak bubble velocities,” [arXiv:1302.1044](#) [hep-ph].
- [12] A. Mégevand, “Friction forces on phase transition fronts,” *JCAP* **1307** (2013) 045, [arXiv:1303.4233](#) [astro-ph.CO].
- [13] J. R. Espinosa, B. Gripiaios, T. Konstandin, and F. Riva, “Electroweak Baryogenesis in Non-minimal Composite Higgs Models,” *JCAP* **1201** (2012) 012, [arXiv:1110.2876](#) [hep-ph].
- [14] J. R. Espinosa, T. Konstandin, and F. Riva, “Strong Electroweak Phase Transitions in the Standard Model with a Singlet,” *Nucl. Phys.* **B854** (2012) 592–630, [arXiv:1107.5441](#) [hep-ph].
- [15] T. Konstandin, G. Nardini, and I. Rues, “From Boltzmann equations to steady wall velocities,” *JCAP* **1409** no. 09, (2014) 028, [arXiv:1407.3132](#) [hep-ph].
- [16] J. Kozaczuk, “Bubble Expansion and the Viability of Singlet-Driven Electroweak Baryogenesis,” *JHEP* **10** (2015) 135, [arXiv:1506.04741](#) [hep-ph].

- [17] M. Quiros, “Finite temperature field theory and phase transitions,” in *Proceedings, Summer School in High-energy physics and cosmology: Trieste, Italy, June 29-July 17, 1998*, pp. 187–259. 1999. [arXiv:hep-ph/9901312](#) [hep-ph].
- [18] C. L. Wainwright, “CosmoTransitions: Computing Cosmological Phase Transition Temperatures and Bubble Profiles with Multiple Fields,” *Comput. Phys. Commun.* **183** (2012) 2006–2013, [arXiv:1109.4189](#) [hep-ph].
- [19] G. D. Moore, “Measuring the broken phase sphaleron rate nonperturbatively,” *Phys. Rev.* **D59** (1999) 014503, [arXiv:hep-ph/9805264](#) [hep-ph].
- [20] B. Laurent, J. Cline, A. Friedlander, D.-M. He, K. Kainulainen, and D. Tucker-Smith, “Baryogenesis and gravity waves from a strong electroweak phase transition,” (In preparation) .
- [21] G. D. Moore, “Electroweak bubble wall friction: Analytic results,” *JHEP* **03** (2000) 006, [arXiv:hep-ph/0001274](#).
- [22] B. Laurent and J. M. Cline, “Fluid equations for fast-moving electroweak bubble walls,” [arXiv:2007.10935](#) [hep-ph].
- [23] W. H. Press, S. A. Teukolsky, W. T. Vetterling, and B. P. Flannery, *Numerical Recipes in C*. Cambridge University Press, Cambridge, USA, second ed., 1992.
- [24] **ATLAS** Collaboration, M. Aaboud *et al.*, “Combination of searches for invisible Higgs boson decays with the ATLAS experiment,” *Phys. Rev. Lett.* **122** no. 23, (2019) 231801, [arXiv:1904.05105](#) [hep-ex].
- [25] N. Craig, H. K. Lou, M. McCullough, and A. Thalapillil, “The Higgs Portal Above Threshold,” *JHEP* **02** (2016) 127, [arXiv:1412.0258](#) [hep-ph].
- [26] **LUX** Collaboration, D. Akerib *et al.*, “First results from the LUX dark matter experiment at the Sanford Underground Research Facility,” *Phys. Rev. Lett.* **112** (2014) 091303, [arXiv:1310.8214](#) [astro-ph.CO].
- [27] G. Guennebaud, B. Jacob, *et al.*, “Eigen v3.” [Http://eigen.tuxfamily.org](http://eigen.tuxfamily.org), 2010.
- [28] M. Galassi, J. Davies, J. Theiler, B. Gough, G. Jungman, M. Booth, and F. Rossi, “Gnu scientific library - reference manual.”
- [29] R. R. Parwani, “Resummation in a hot scalar field theory,” *Phys. Rev. D* **45** (1992) 4695, [arXiv:hep-ph/9204216](#). [Erratum: *Phys.Rev.D* 48, 5965 (1993)].
- [30] D. Curtin, P. Meade, and H. Ramani, “Thermal Resummation and Phase Transitions,” *Eur. Phys. J. C* **78** no. 9, (2018) 787, [arXiv:1612.00466](#) [hep-ph].
- [31] J. M. Cline and P.-A. Lemieux, “Electroweak phase transition in two Higgs doublet models,” *Phys. Rev.* **D55** (1997) 3873–3881, [arXiv:hep-ph/9609240](#) [hep-ph].